

## Article

# Study on the Contamination Characteristics of V-Type Double Suspension Rod Insulators Based on the Influence of Wake Flow

Shanpeng Zhao , Tianyu Wang , Youpeng Zhang and Yuantao Liu 

School of Automation and Electrical Engineering, Lanzhou Jiaotong University, Lanzhou 730070, China

\* Correspondence: zsp@mail.lzjtu.cn

**Abstract:** The insulators of the catenary of the Lanzhou-Xinjiang High-speed Railway in windy areas suffer from serious contamination, which has led to frequent flashover accidents. The catenary of the Lanzhou-Xinjiang High-speed Railway has adopted the unique external insulation of V-type double suspension rod insulators. To further determine the contamination characteristics of this type of insulator, a contamination simulation model of insulator is established in this paper based on the principles of fluid mechanics, which is used to analyze the contamination characteristics of the V-type double suspension rod insulators under the influence of wake flow. The research results show that wind speed directly determines the static pressure on the surface of the insulator, the wind speed and particle concentration are proportional to the contamination volumes on the windward and crosswind sides of insulator, while the particle size is inversely proportional to the contamination volume on the leeward side of the insulator. The direction of wake flow is consistent with the direction angle of external incoming flow, and the wake flow generating area affects the contamination characteristics of the insulator. When the incoming flow is at a prevailing wind direction of  $0^\circ$ , focus should be put on the windward and crosswind sides of the two insulators during insulator cleaning, and the contamination distributions on these two insulators are similar; when the incoming flow is at a prevailing wind elevation of  $0^\circ \sim 60^\circ$ , focus should be put on the entire surface of 1# insulator and the windward and crosswind sides of 2# insulator during insulator cleaning.

**Keywords:** V-type double suspension rod insulators; fluid mechanics; static pressure on surface; contamination volume fraction; impact of wake flow; contamination characteristics



**Citation:** Zhao, S.; Wang, T.; Zhang, Y.; Liu, Y. Study on the Contamination Characteristics of V-Type Double Suspension Rod Insulators Based on the Influence of Wake Flow. *Coatings* **2022**, *12*, 1262. <https://doi.org/10.3390/coatings12091262>

Academic Editor: Ioannis Karapanagiotis

Received: 30 June 2022

Accepted: 21 August 2022

Published: 29 August 2022

**Publisher's Note:** MDPI stays neutral with regard to jurisdictional claims in published maps and institutional affiliations.



**Copyright:** © 2022 by the authors. Licensee MDPI, Basel, Switzerland. This article is an open access article distributed under the terms and conditions of the Creative Commons Attribution (CC BY) license (<https://creativecommons.org/licenses/by/4.0/>).

## 1. Introduction

The Lanzhou-Xinjiang High-speed Railway is the first high-speed railway across the entire areas of Gansu and Xinjiang in China, which has a length of about 1775 km. Along the Lanzhou-Xinjiang High-speed Railway, there are several windy areas in Xinjiang. Among them, there is a “100 km wind area” with a total length of about 100 km where strong winds blow for more than 320 days per year. The dust and other dirty particles carried by the strong wind tend to attach to the surface of the catenary insulator along the railway, which leads to the hidden danger of contamination flashover discharge of the insulator for large areas [1–5], thus threatening the safety of railway transportation. To alleviate the drastic galloping of the positive feeder in the highly windy environment, the V-type double suspension is adopted for installation of the insulators connected to the positive feeder. The unique triangular structure of V-type double suspension is utilized to increase the suspension stability. The catenary environment is shown in Figure 1. Because of the unique structure of the V-type double suspension rod insulators, the two insulators present different contamination characteristics under the influence of wake flow. The conventional insulator contamination theory and prediction model cannot well explain and predict these contamination characteristics, and the maintenance period of the V-type double suspension rod insulators is also different from that of the conventional insulator. Therefore, study on

the contamination characteristics of V-type double suspension rod insulators is of great guiding significance for expanding the theoretical research of insulator contamination and controlling the contamination of insulators on site. The V-type double suspension rod insulators include two insulators, named 1# insulator and 2# insulator, respectively. The two insulators are presented in Figure 2.

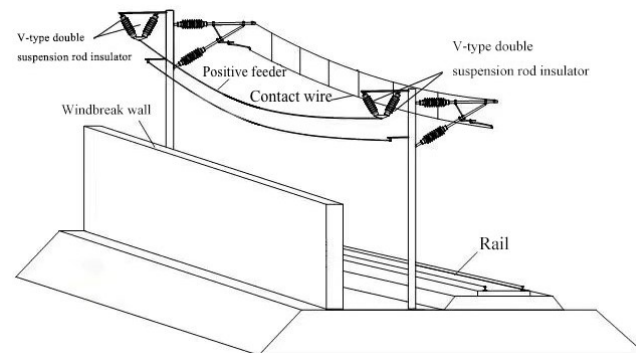


**Figure 1.** Diagram of catenary environment.

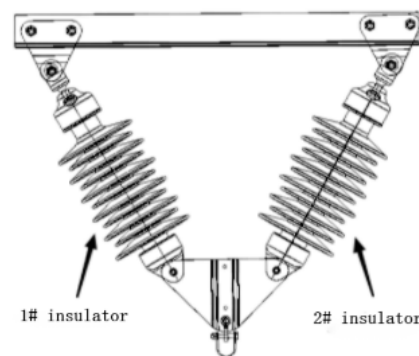


**Figure 2.** Diagram of two numbered insulators.

Many scholars have conducted in-depth researches on insulator contamination [6–9], and analyzed the impact of insulator contamination on contamination flashover. Shariati et al. [10] studied the contamination flashover characteristics of insulators, and in their study, when the insulator surface was wet due to rain or fog, the contamination deposits would accumulate on the insulator surface and become a conductive path, eventually leading to flashover. Yang Zhongyi et al. [11] studied the effect of the chemical composition of contamination on the flashover performance of insulators made of different materials. Their research demonstrates that when the insulators of different materials were contaminated, the ion concentrations on their surfaces were different, and the flashover gradient was positively correlated with the ion concentration. At the same time, some other scholars used intelligent methods, such as neural network and particle swarm, to predict and evaluate the contamination degree, leakage current and contamination flashover of insulators, which presented good application values. For example, V.T. Kontargyri et al. [12] used an artificial neural network model to predict the critical flashover voltage of contaminated insulators. In their work, when using this model, the actual parameters of the insulator were used as the input variables to predict the critical flashover voltage, and the obtained results were efficient and accurate. Shariatinasia et al. [13] proposed a probabilistic method based on the finite element method (FEM) to simulate the insulator flashover and calculate the failure risk of insulators under contaminated conditions, and their research results can be used as reference to determine the replacement intervals of insulators. Vita V et al. [14] used an artificial neural network model to evaluate the contamination level of insulators, and the results obtained using the proposed artificial neural network were very close to the

actual results, with acceptable accuracy. Phuong Nguyen Thanh et al. [15] utilized the surface spark discharge data and the neural network based on particle swarm optimization to predict the leakage current of insulators. Their research shows that a high accuracy can be achieved in predicting the leakage current of insulators by combining particle swarm optimization with the neural network algorithm. Sid Ahmed Bessedik et al. [16] used the least squares support vector machine (LS-SVM) of particle swarm optimization to predict the flashover voltage of insulators. The results of their study show that particle swarm optimization can be used to automatically adjust the parameters of LS-SVM, and more accurate results can be obtained by using this model in predicting the critical flashover voltage of insulators.

Some scholars proved that the surface salt density of insulators is closely related to the environmental humidity, through research. Zhang Chuyan et al. [17] studied the contamination deposition characteristics of insulators in a hazy environment. Their findings show that the higher the environmental humidity of the insulators was, the faster the contamination accumulation on the insulators, and the equivalent salt deposition density (ESDD) on the surface increased linearly with the increase of haze conductivity. Jiang Zidan et al. [18] studied the law of natural contamination on the insulator surface in rainy weather. The study shows that the residual ESDD and non-soluble deposit density (NSDD) on the surface of insulators were affected by the rainfall intensity, duration and flushing angle. Some other scholars studied the contamination accumulation characteristics of insulators in different forms [19–21] and the influence of the flow field on contamination accumulation. For instance, Li Lee et al. [22] studied the contamination characteristics of insulators on the DC ultra-high voltage and AC ultra-high voltage transmission lines, and found that anions, cations and charges played an important role in the contamination accumulation of insulators. Gao Bing et al. [23] studied the influence of charged haze particles on the contamination accumulation of insulators. In their research, driven by the electric field force, the movement path of charged haze particles would deflect along the electric field lines, which would accelerate the precipitation of haze particles on the DC insulators. Yang Jiaxin et al. [24] used the characteristic particle tracking method to calculate the contamination accumulation of insulators. The study shows that the surface area of an insulator is determined by the electric field strength, wind speed and other factors. Li Te et al. [25] studied the difference in the contamination characteristics between the composite rod insulator and the standard disc suspension insulator, and found that the contamination difference between the upper and lower surfaces of composite insulator was smaller than that of standard suspension insulators. Huang Yanchen et al. [26] investigated the relationship between the contamination accumulation on the insulator surface and the distribution of the flow field around the insulator. In their work, when the wind speed was 3~7 m/s, there was obvious separation of the boundary layer, and the contamination accumulation on the insulator surface was closely related to the distribution of the flow field around the insulator.

To sum up, many in-depth studies on the contamination accumulation of insulators have been carried out, and fruitful results have been achieved. On the basis of understanding the influence of insulator contamination accumulation on flashover, intelligent algorithms can be used to predict and evaluate the insulator state. The contamination accumulation of insulators is not only affected by its own structure and surface material, but is also closely related to factors such as the wind environment, air humidity, and particulate parameters. Moreover, the research objects in these works are all single insulators, but two insulators are often combined in the field. In some wind directions, one insulator will affect the flow field of the other insulator, thus changing the contamination characteristics of the insulators. In addition to understanding the contamination characteristics of a single insulator of the same type, it is also necessary to study the contamination characteristics of two insulators in joint application based on the influencing factors of wake flow.

In this paper, based on the principle of fluid mechanics, the flow field simulation model of V-type double suspension insulators for the OCS of Lanzhou-Xinjiang High-

speed Railway is established, and the mesh is divided. Combined with the influence of insulator wake, the velocity distribution of V-type double suspension insulators under different wind speed, inflow angle, particle size and particle concentration is studied, and the contamination accumulation characteristics of the insulator are analyzed.

## 2. Principle of Euler Two-Phase Flow Simulation in Fluid Mechanics

### 2.1. Basic Equation

The insulator is located in a fluid area where many kinds of particles are mixed with air [27]. The insulator has a structure similar to a cylinder, which is called a bluff-body in fluid mechanics, and the bluff-body structure interacts with the wind to produce a wake flow. This paper investigates the contamination characteristics under the influence of wake flow, so it is necessary to analyze the interactions between particles and insulator the flow field. By maintaining the volume fraction of the total number of phases in the entire computational domain as 1, the particle group composed of gas and different contamination particles in the computational domain is regarded as two kinds of fluids. Under strong wind, when the air and the particle group in the air act on the 1# insulator, the primary wake flow will be generated; then, the primary wake flow drives the particle group to continue to move backward and act on the 2# insulator, resulting in a secondary wake flow. In this paper, the contamination characteristics on the insulator surface under the influence of the wake flow are analyzed according to the principles of Euler two-phase flow.

Euler's differential equation of motion is:

$$\begin{aligned} & (Xdx + Ydy + Zdz) - \frac{1}{\rho} \left( \frac{\partial p}{\partial x} dx + \frac{\partial p}{\partial y} dy + \frac{\partial p}{\partial z} dz \right) \\ & = \frac{du_x}{dt} dx + \frac{du_y}{dt} dy + \frac{du_z}{dt} dz \end{aligned} \quad (1)$$

where  $dx$  is the coordinate component of the distance between any two points in the flow field in the  $x$ -axis direction;  $dy$  is the coordinate component of the distance between any two points in the flow field in the  $y$ -axis direction;  $dz$  is the coordinate component of the distance between any two points in the flow field in the  $z$ -axis direction;  $\rho$  is the relative density of the flow field;  $\partial p$  is the volume fraction of the  $p$ -th phase in the fluid;  $\frac{du_x}{dt}$  is the velocity gradient of the fluid in the  $x$ -axis direction;  $\frac{du_y}{dt}$  is the velocity gradient of the fluid in the  $y$ -axis direction;  $\frac{du_z}{dt}$  is the velocity gradient of the fluid in the  $z$ -axis direction.

Simplify (1) to get:

$$\begin{cases} X + Y + Z = W \\ (Xdx + Ydy + Zdz) = dW = -gdz \\ \frac{1}{\rho} \left( \frac{\partial p}{\partial x} dx + \frac{\partial p}{\partial y} dy + \frac{\partial p}{\partial z} dz \right) = \frac{1}{\rho} dp \\ \frac{du_x}{dt} dx + \frac{du_y}{dt} dy + \frac{du_z}{dt} dz = d\left(\frac{u^2}{2}\right) \end{cases} \quad (2)$$

where  $W$  is the potential function. When the Euler equation of motion satisfies the above formula, the fluid movement is only affected by its gravity and the acting force of the insulator, the streamline coincides with the trace in the fluid, and the movement remains unchanged along the same streamline, resulting in wake flow.

Solving (2), we can obtain:

$$-g dz - \frac{1}{\rho} dp = d\left(\frac{u^2}{2}\right) \quad (3)$$

Convert (3) into an integrable form:

$$dW - d\left(\frac{p}{\rho}\right) = d\left(\frac{u^2}{2}\right) \quad (4)$$

Integrate (4) to get:

$$-gz - \frac{p}{\rho} - \frac{u^2}{2} = Cl \quad (5)$$

where,  $Cl$  is the streamline constant, and because the fluid is incompressible,  $\rho = C$ . Let  $\gamma = \frac{\rho}{g}$ , simplify (5) to get the Bernoulli equation for ideal potential flow:

$$z + \frac{p}{\gamma} + \frac{u^2}{2g} = C \quad (6)$$

where,  $z$  is the potential energy per unit weight of the fluid;  $\frac{p}{\gamma}$  is the pressure energy per unit weight of fluid;  $\frac{u^2}{2g}$  is the kinetic energy per unit weight of the fluid;  $C$  is the Bernoulli constant.

The fluid domain satisfies the Bernoulli equation for ideal potential flow [28], and a constant flow acts on a compressible or incompressible fluid, which satisfies the motion principle of Euler two-phase flow. The two-phase flow model was used in the simulation experiments, while the Euler two-phase flow method was employed to perform fluid mechanics continuity calculation by using two-phase fluid.

The continuity equation for the two-phase fluid is:

$$\frac{1}{\rho_{rv}} \left( \frac{\partial \alpha_v \rho_v}{\partial t} + \nabla \cdot (\alpha_v \rho_v \vec{v}_v) \right) = \sum_{\rho=1}^n (\dot{m}_{uv} - \dot{m}_{vu}) + S_v \quad (7)$$

where  $\rho_{rv}$  is the phase density of the fluid;  $\alpha_v$  is the volume fraction of the  $v$ -th phase in the fluid;  $\rho_v$  is the relative density of the  $v$ -th phase in the fluid;  $\vec{v}_v$  is the velocity of the  $v$ -th phase in the fluid;  $\dot{m}_{uv}$  is the mass difference moving from the  $u$ -th phase to the  $v$ -th phase in the fluid;  $\dot{m}_{vu}$  is the mass difference moving from the  $v$ -th phase to the  $u$ -th phase in the fluid;  $S_v$  is the source item, and the default value is 0.

To calculate complex models in viscous fluid, the RNG  $k - \epsilon$  model is used to simulate and solve the model in the simulation stage.

The  $k$  equation is:

$$\frac{\partial(\rho k)}{\partial t} + \frac{\partial(\rho k u_i)}{\partial x_i} = \frac{\partial}{\partial x_j} \left( \alpha_k \mu_{eff} \frac{\partial k}{\partial x_j} \right) + G_k + \rho \epsilon \quad (8)$$

The  $\epsilon$  equation is:

$$\frac{\partial(\rho \epsilon)}{\partial t} + \frac{\partial(\rho \epsilon u_i)}{\partial x_i} = \frac{\partial}{\partial x_j} \left( \alpha_\epsilon \mu_{eff} \frac{\partial \epsilon}{\partial x_j} \right) + \frac{C_{1\epsilon} \epsilon}{k} G_k - \frac{C_{2\epsilon} \rho \epsilon^2}{k} \quad (9)$$

where  $G_k$  is the turbulence kinetic energy generated by the fluid motion;  $\alpha_k$  is the Prandtl number of the turbulence kinetic energy  $k$ ;  $\alpha_\epsilon$  is the Prandtl number of the dissipation rate  $\epsilon$ ;  $C_{1\epsilon}$  and  $C_{2\epsilon}$  are empirical constants;  $\mu_{eff}$  is the turbulent viscosity coefficient.

## 2.2. Model Building and Meshing

In this paper, simulation research is carried out with the V-type double suspension rod insulators installed on the column of the Lanzhou-Xinjiang High-speed Railway catenary as the research object. See Figure 3 for the insulator structure and related parameters. The insulating part of the insulator is made of composite material, and the system mainly consists of the following five parts: a V-shaped suspension shoulder frame on the top of the positive feeder column, a grooved ball head, a rod-type suspension insulator, a two-ear yoke plate, and a D-type connector. Among them, the rod-type suspension insulator includes six big sheds and five small sheds, and the diameters of the big shed and small shed are 160 mm and 120 mm, respectively. The vertical distance of the insulator is 865 mm, and the creep distance is 1730 mm.

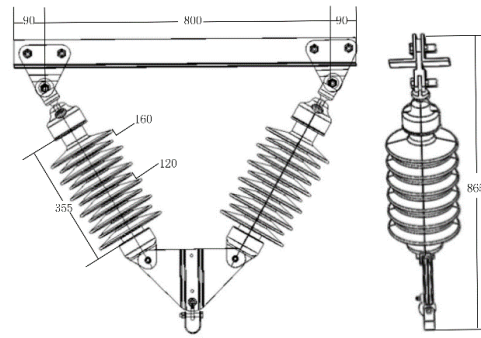


**Figure 3.** Structural diagram of V-type double suspension rod insulators.

First, a three-dimensional model should be built using the SolidWorks software. Because an external spatial computational domain should be constructed to ensure that the wind speed can cause turbulence in the simulation, it is necessary to use the blocking rate in fluid mechanics as a reference factor, and the blocking rate should be less than 5%.

The blocking rate  $\zeta$  is defined as:

$$\zeta = \frac{L_1}{L} \quad (10)$$

where,  $L_1$  is the projected area of the model in the direction facing the inlet of spatial computational domain,  $\text{m}^2$ ;  $L$  is the cross-sectional area in the direction of the inlet of spatial computational domain,  $\text{m}^2$ .

In this paper, because the insulator has a unique structure similar to the equilateral triangle structure, to ensure that the model is under even impact from the incoming current and the wake flow, the spatial computational domain model is set as a cube model with a size of  $3000 \text{ mm} \times 3000 \text{ mm} \times 3000 \text{ mm}$ . According to the calculation results of the shed part of the three-dimensional insulator model, as shown in Figure 4, when the incoming flow is in the  $x$  direction:  $D_{rx} = 0.16 \text{ m} \times 0.35 \text{ m} \times 2 = 0.112 \text{ m}^2$ ; when the incoming flow is in the  $y$  direction:  $D_{ry} = 0.16 \text{ m} \times 0.35 \text{ m} = 0.112 \text{ m}^2$ . The cross-sectional area in the direction of the inlet of the computational domain is defined as:  $3000 \text{ mm} \times 3000 \text{ mm} = 9 \text{ m}^2$ , and the calculated blocking rates are 0.012 and 0.006, respectively. The mesh mainly consists of the two parts of the external spatial computational domain and the internal insulator, meshing should be performed on these two parts, and measures should be taken to avoid mesh reconstruction [29]. The coordinate system of the insulator model is shown in Figure 4, and the meshing of the model is shown in Figure 5. The model is composed of unstructured meshes, and the total number of meshes is about 3.8 million.

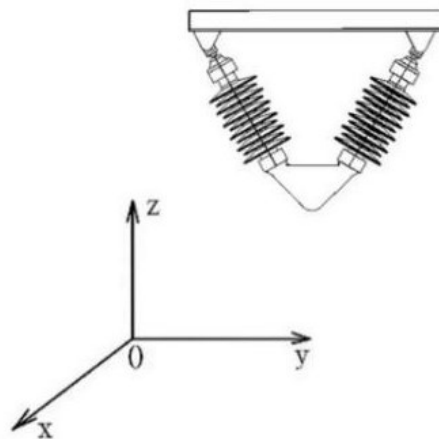


**Figure 4.** Coordinate system of the insulator model.

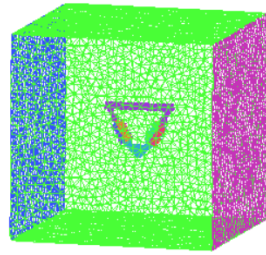


**Figure 5.** Meshing of the model.

### 2.3. Settings of Boundary Conditions for Simulation

The fluid mechanics simulation was performed using the Fluent software. After importing the model into the external spatial computational domain, three boundary conditions should be set. As shown in Figure 5, the blue part on the left side of the computational domain is defined as the boundary conditions for the incoming flow velocity at inlet (Velocity\_inlet); the purple part on the right side of the computational domain is defined as the boundary conditions for the outflow velocity at outlet (Out\_flow); the green part of the computational domain is defined as the boundary conditions of wall (Wall). The turbulence intensity  $I$  and hydraulic diameter  $D$  should be considered for the inlet and outlet velocities of the computational domain.

The expression is:

$$\begin{cases} I = 0.16(Re)^{-\frac{1}{8}} \\ D = \frac{4L}{d} \end{cases} \quad (11)$$

where  $d$  is the perimeter of the inlet of the computational domain, m;  $Re$  is the Reynolds number.

The equation of the Reynolds number is:

$$Re = \frac{\rho v D}{\eta} \quad (12)$$

where  $v$  is the fluid velocity, m/s;  $\eta$  is the fluid viscosity, m<sup>2</sup>/s.

Each insulator shed is divided into three parts: the windward side, the leeward side, and the crosswind side. The diagram of the shed division is shown in Figure 6.

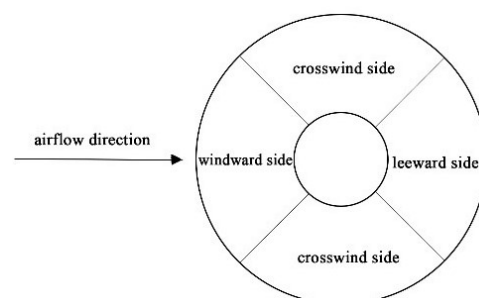


**Figure 6.** Schematic diagram of the shed division of insulator.

After field investigation of the sandstorm environment of the Lanzhou-Xinjiang High-speed Railway, the sizes of contamination particles at both ends of the insulator under different voltages in an artificial environment are analyzed according to the contamination patterns of insulators in the natural environment [30]. The contamination particles present a normal distribution on the insulator surface; and the contaminated particle sizes are set to 10  $\mu\text{m}$ , 15  $\mu\text{m}$ , 20  $\mu\text{m}$ , and 25  $\mu\text{m}$ , respectively. In this paper, the calcium carbonate model is employed to simulate the contamination particles. The relative density of particles is

2800 kg/m<sup>3</sup>. The main relative density of air is set at 1.29 kg/m<sup>3</sup>, and the concentrations of contamination particles are set as 0.02 mg/m<sup>3</sup>, 0.04 mg/m<sup>3</sup>, 0.06 mg/m<sup>3</sup>, 0.08 mg/m<sup>3</sup> and 0.1 mg/m<sup>3</sup>, respectively. The wind speed of the Lanzhou-Xinjiang High-speed Railway is generally at level 7–8 in the windy areas, so the wind speeds are set as 10 m/s, 15 m/s, 20 m/s, and 25 m/s, respectively. The wind attack angle at the positive feeder is changed due to the shielding of the wind-break wall, and the wake flow trajectories generated by the insulator under different wind angles are also different. In order to study the angle and continuation direction of wake flow, the angles of incoming flow are set to be within the following ranges:

- (1) ① Wind direction of 0°: horizontal wind blows vertically to the  $x = 0$  plane.  
 ② Wind direction of 90°: horizontal wind blows vertically to the  $y = 0$  plane.

- (2) ① Wind elevation of 0°: horizontal wind blows vertically to the  $y = 0$  plane (wind direction of 90°). ② Wind elevation of 30°: the wind angle is 30° upward from the horizontal plane. ③ Wind elevation of 45°: the wind angle is 45° upward from the horizontal plane. ④ Wind elevation of 60°: the wind angle is 60° upward from the horizontal plane.

With the meshes of internal insulator maintained, the angle of the meshes of external spatial domain is changed, and different incoming flow angles are set. The schematic diagrams under different wind direction angles are shown in Figure 7, and the diagrams under different wind elevation angles are shown in Figure 8.

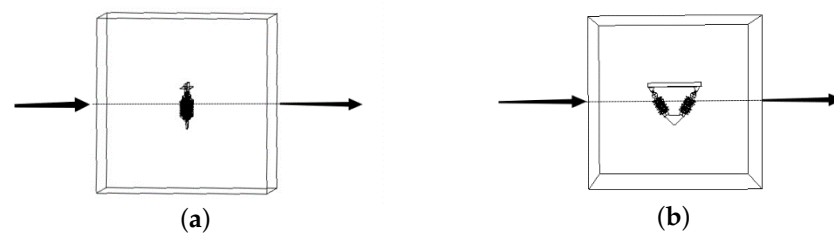


**Figure 7.** Schematic diagrams under different wind direction angles (horizontal wind). (a) 0° wind direction angle; (b) 90° wind direction angle (wind elevation of 0°).

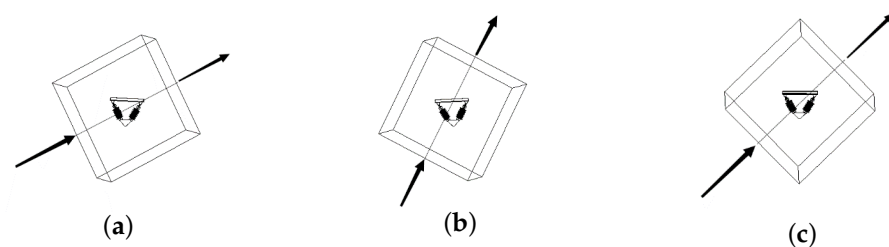


**Figure 8.** Schematic diagrams under different wind elevation angles. (a) 30° wind elevation angle; (b) 45° wind elevation angle; (c) 60° wind elevation angle.

### 3. Flow Field Analysis of Insulator

#### 3.1. Pressure Distribution on the Insulator Surface

The influence of the wake flow generated by the bluff-body structure of 1# insulator on 2# insulator can't be analyzed when the incoming flow is at wind direction of 0°, so the pressure distribution on the insulator surface is analyzed under the incoming flow at wind direction of 90°. The pressure distribution pattern on the model surface under the influence of wake flow is examined. When the wind speed is 10 m/s, 15 m/s, 20 m/s, and 25 m/s, the surface pressure distributions on the crosswind side of insulators, the windward surface of 2# insulator, the windward surface of 1# insulator, the leeward surface of 2# insulator and the leeward surface of 1# insulator are shown in Figures 9a–e, 10a–e, 11a–e and 12a–e, respectively. The simulation conditions are as follows: the particle size is 15 μm, the particle concentration is 0.02 mg/m<sup>3</sup>, and the incoming flow is at the wind direction of 90°.

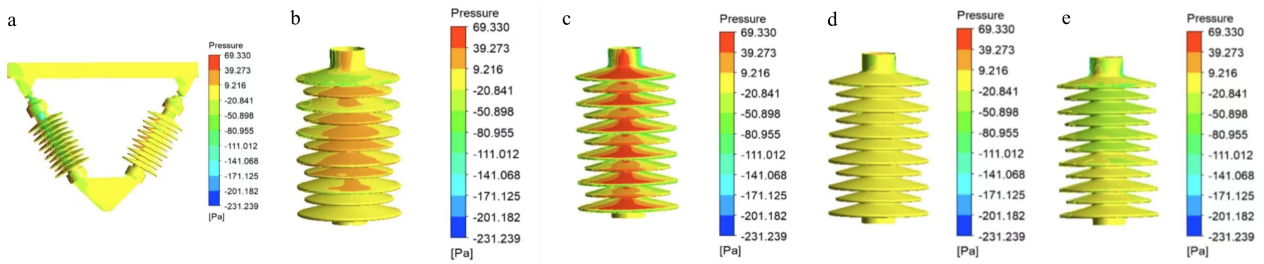


**Figure 9.** Static pressure distributions on the insulator surface under the wind speed of 10 m/s. (a) the surface pressure distributions on the crosswind side of insulators; (b) the surface pressure distributions on the windward surface of # insulator; (c) the surface pressure distributions on the windward surface of 1# insulator; (d) the surface pressure distributions on the leeward surface of 2# insulator; (e) the surface pressure distributions on the leeward surface of 1# insulator.

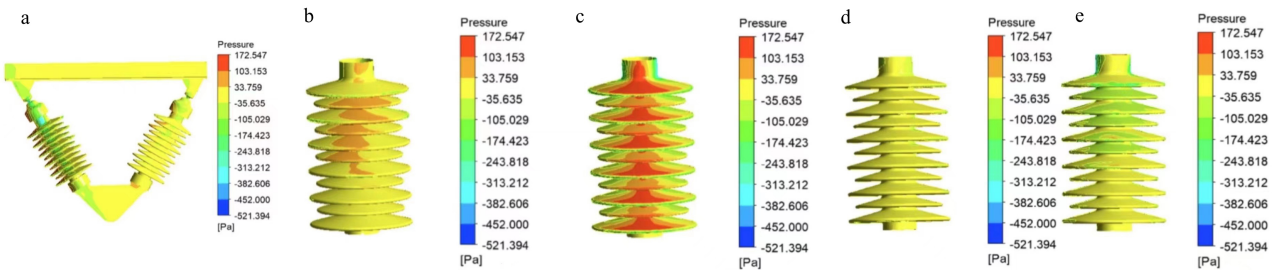


**Figure 10.** Static pressure distributions on the insulator surface under the wind speed of 15 m/s. (a) the surface pressure distributions on the crosswind side of insulators; (b) the surface pressure distributions on the windward surface of 2# insulator; (c) the surface pressure distributions on the windward surface of 1# insulator; (d) the surface pressure distributions on the leeward surface of 2# insulator; (e) the surface pressure distributions on the leeward surface of 1# insulator.

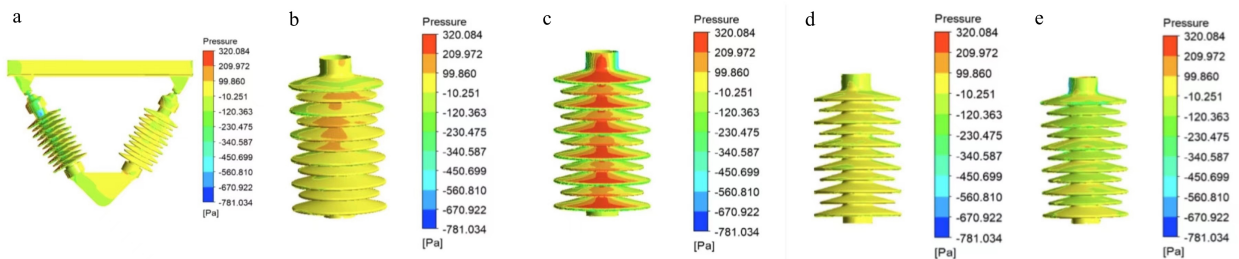


**Figure 11.** Static pressure distributions on the insulator surface under the wind speed of 20 m/s. (a) the surface pressure distributions on the crosswind side of insulators; (b) the surface pressure distributions on the windward surface of 2# insulator; (c) the surface pressure distributions on the windward surface of 1# insulator; (d) the surface pressure distributions on the leeward surface of 2# insulator; (e) the surface pressure distributions on the leeward surface of 1# insulator.

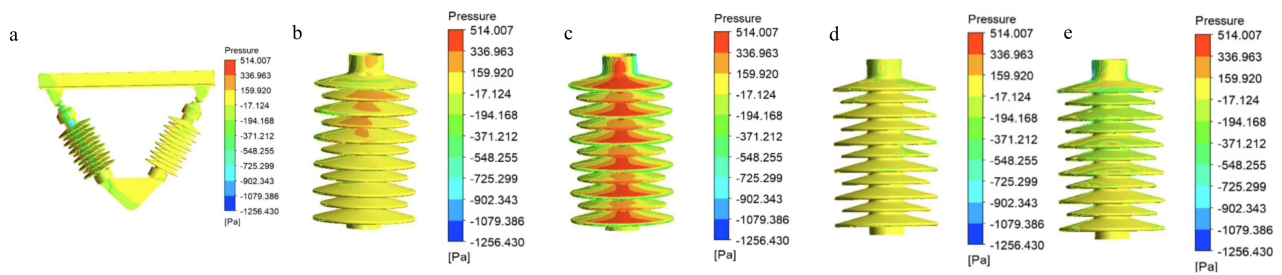


**Figure 12.** Static pressure distributions on the insulator surface under the wind speed of 25 m/s. (a) the surface pressure distributions on the crosswind side of insulators; (b) the surface pressure distributions on the windward surface of 2# insulator; (c) the surface pressure distributions on the windward surface of 1# insulator; (d) the surface pressure distributions on the leeward surface of 2# insulator; (e) the surface pressure distributions on the leeward surface of 1# insulator.

When the incoming flow is at the wind direction of  $90^\circ$ , Figures 9a, 10a, 11a and 12a show that the surface pressure distributions on the overall crosswind side of the insulators under the four different wind speeds are close. The insulator has a structure similar to a cylinder, which is called a bluff body in fluid mechanics, and the bluff-body structure interacts with the wind to produce a wake flow. A primary wake flow is generated on the leeward side of the 1# insulator, the contamination particles on the crosswind side will be blown to the 2# insulator with the wake flow, and as a result, the surface pressure on the crosswind side of the 1# insulator is smaller than that on the windward side of the 2# insulator. As the wind speed gradually increases, the pressure on the windward surface of the 1# insulator gradually increases, but its growth rate shows a decrease trend. According to Figures 9c, 10c, 11c and 12c, the incoming flow contacts the 1# insulator first, the surface pressure of the front end of the shed is about 1.5–2 times higher than the pressure on both sides and the rear end, the contamination particles are brought from the front end of the insulator to the side and the rear end under the influence of the wake flow, and the high-pressure area is extended to the rear end in a crescent shape. According to Figures 9e, 10e, 11e and 12e, because the 1# insulator generates the primary wake flow, the contamination particles on the crosswind side fall off and are blown to the rear part with the strong wind. The vortex turbulence is generated at the leeward side, and the contaminations are piled in the leeward side, causing the pressure on the leeward side of the 1# insulator to be higher than that on its crosswind side. As can be seen from Figures 9b, 10b, 11b and 12b, the windward side of the 2# insulator is affected by the primary wake flow, and a large amount of contamination particles adhere to its windward side, causing the wind pressure on the windward side of 2# insulator to be 1.5–1.8 times higher than that on the other surfaces. With the increase of wind speed, the leeward side of the 2# insulator generates the secondary wake flow, and the vortex turbulence triggered by the primary wake flow gradually loses its balance. When it reaches the critical point, the balance will be destroyed, the contamination particles will be blown away by the strong wind, and the pressure of the windward side of the 2# insulator will gradually decrease. According to Figures 9d, 10d, 11d and 12d, when the secondary wake flow is formed on the leeward side of the 2# insulator, the secondary wake flow gradually weakens because there is no shielding from object behind the 2# insulator, and the adhesion of contamination particles is higher than the gravity. The contamination particles on the crosswind side cannot fall off in large quantities, causing the surface pressure on crosswind side of the 2# insulator to be close to that on the leeward side.

As for the overall surface pressures of insulator, the pressure on the windward side is higher than that on the crosswind and leeward sides, and the pressures on the windward side and leeward side of the 2# insulator are close to each other. The more contamination particles adhere to the insulator, the more violent the collision becomes, and the higher the

surface pressure. The maximum surface pressures on insulators under the wind speeds of 10 m/s, 15 m/s, 20 m/s, and 25 m/s are 69.3 pa, 172.5 pa, 320 pa and 514 pa, respectively.

### 3.2. External Flow Field Distribution of the Insulator

The contamination particles flow with the airflow outside the insulator, and the external flow field acts on the front end of the insulator to generate a primary wake flow. The contamination particles that originally flowed with the airflow deviate from the original flow track under the influence of the wake flow, and some of them adhere to the insulator surface, while the rest fall off and continue to move backward along with the wake flow and contact the rear end of the insulator to generate a secondary wake flow. Figures 13 and 14 show the cloud maps of the plane velocity distribution of the incoming flow at a 90° wind direction angle when the particle concentration is 0.02 mg/m<sup>3</sup> and the wind speed is 10 m/s and 15 m/s. The insulator wake flow streamline is shown in Figure 15.

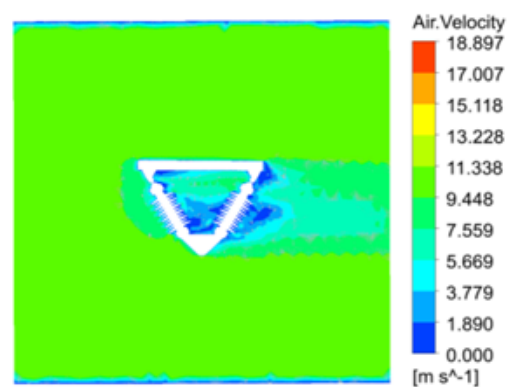


Figure 13. Cloud map of the plane velocity distribution under the wind speed of 10 m/s.

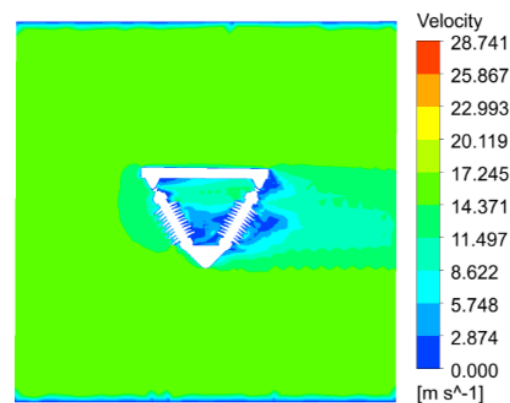


Figure 14. Cloud map of the plane velocity distribution under the wind speed of 15 m/s.

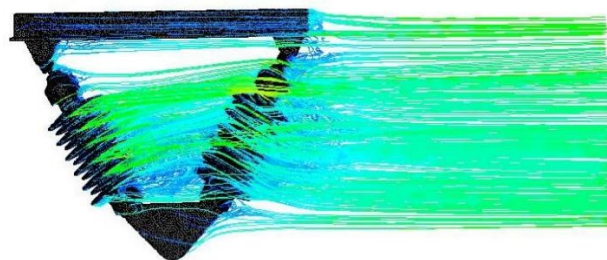


Figure 15. Wake streamline diagram.

In Figures 13 and 14, the light blue area on the left side of the 1# insulator is where the airflow carrying contamination particles first contacts with the insulator, and this area has a boundary layer [31]. After the contamination particles enter the boundary layer, some are attached to the surface of the insulator, and some continue to flow to the rear end with the airflow. When the strong airflow acts on the 1# insulator, the laminar flow on the leeward side of the 1# insulator is destroyed, forming vortex turbulence, and generating the primary wake flow, and this is the dark blue area in the middle of the two insulators in Figures 13 and 14. At this point, the wind speed is decreasing. The contamination particles adhered to the side of the 1# insulator peel off due to the influence of the primary wake flow, continue to move to the rear end with the wake flow and adhere to the windward side of the 2# insulator. The primary wake flow works on the 2# insulator and generates the secondary wake flow, which is the dark blue area on the right side of the 2# insulator in Figures 13 and 14. The secondary wake flow weakens and gradually returns to advection because there is no shield behind the 2# insulator. Most of the contamination particles can't continue to adhere to the leeward side of the 2# insulator, so they fall off from the insulator. At this point, the wind speed on the leeward side of the 2# insulator is the lowest. The fallen off contamination particles leave the wake flow area with the wind, and the wind speed gradually increases and returns to the speed when touching the 1# insulator, which is the light blue area on the right side of the 2# insulator in Figures 13 and 14. As shown in Figure 15, the wake flow is shown in the form of a streamline. Vortex turbulence is formed on the leeward side of 1# insulator and 2# insulator. The primary wake flow affects the surface contamination characteristics of insulator 2#. As there is no shield behind insulator 2#, the secondary wake flow continuously weakens until it disappears and becomes a model of normal laminar flow.

#### 4. Analysis of Contamination Characteristics of Insulators under Different Influencing Factors

##### 4.1. Definition of Contamination Volume Fraction

In this paper, the contamination volume fraction is used as a characterization parameter to analyze the contamination characteristics of insulators under different influence conditions.

The contamination volume fraction  $\phi$  is expressed as follows:

$$\phi = \frac{V_{\text{particle}}}{V_{\text{particle}} + V_{\text{air}}} \quad (13)$$

where,  $V_{\text{particle}}$  is the contamination volume,  $\text{m}^3$ ;  $V_{\text{air}}$  is the total volume of air,  $\text{m}^3$ . The area-weighted means of the contamination volume fractions of different parts (such as the windward side, the crosswind side, and the leeward side) represent the contamination degree each part, and its expression  $\phi_{\text{ave}}$  is:

$$\phi_{\text{ave}} = \frac{1}{A} \int \phi dA = \frac{1}{A} \sum_{i=1}^n \phi_i A_i \quad (14)$$

where,  $A$  is the area of the selected part;  $n$  is a discrete quantity on  $A$ ;  $\phi_i$  is the contamination volume fraction in the mesh nodes;  $A_i$  is the microelement area.

##### 4.2. Different Concentrations of Contamination Particles

The Lanzhou-Xinjiang High-speed Railway is located in an area with frequent wind and sand weathers, and the concentrations of contamination particles in the air are different. With the particle concentrations of  $0.04 \text{ mg/m}^3$ ,  $0.06 \text{ mg/m}^3$ , and  $0.1 \text{ mg/m}^3$  as examples the contamination distribution on insulators is analyzed. The simulation conditions are set as follows: the particle size is  $15 \text{ }\mu\text{m}$ , the wind speed is  $20 \text{ m/s}$ , and the incoming flow is at the wind direction of  $90^\circ$ . Figures 16–18 show the contamination distribution on the insulator surface at concentrations of  $0.04 \text{ mg/m}^3$ ,  $0.06 \text{ mg/m}^3$ , and  $0.1 \text{ mg/m}^3$ . Figure 19

shows the curve of how the overall surface contamination volume fractions of 1# insulator and 2# insulator change with the concentrations of contamination particles.

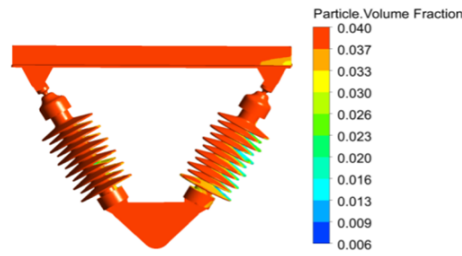


Figure 16. Distribution map of contamination on the surface of insulators with a concentration of 0.06 mg/m<sup>3</sup>.

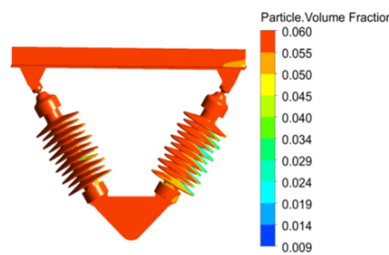


Figure 17. Distribution map of contamination on the surface of insulators with a concentration of 0.04 mg/m<sup>3</sup>.

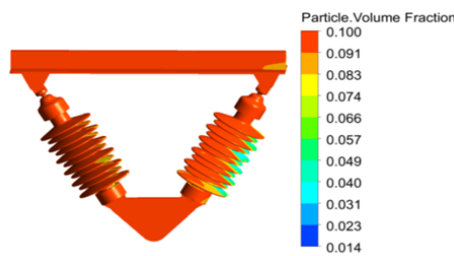


Figure 18. Distribution map of contamination on the surface of insulators with a concentration of 0.1 mg/m<sup>3</sup>.

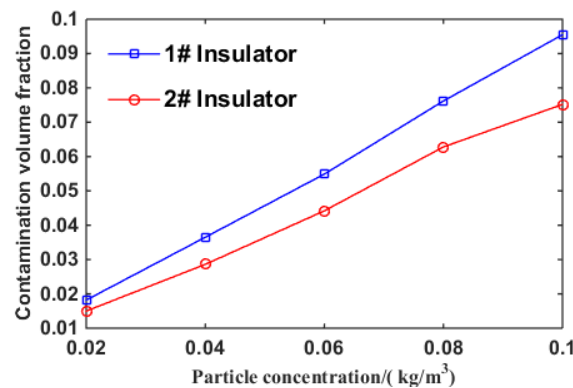


Figure 19. Variation of contamination of volume fraction with particle concentration.

The contamination volume fraction on the insulator surface increases with the increase of the contamination particle concentration in the air, and the contamination content on the leeward side of the 2# insulator is the lowest. From the curve in Figure 19, it can be seen that the contamination volume fractions of 1# insulator and 2# insulator increase linearly in general, from 0.01 to about 0.09. The contamination particle concentration

in the air increases, and the proportion of contamination particles in the air increases, which will make it easier for particles to attach to the insulator surface. The primary wake flow gradually strengthens. With the increase of particle concentration, the contamination particles on the surface of the 1# insulator gradually accumulate, and the contamination volume fraction of the 1# insulator shows an increasing trend; the secondary wake flow gradually weakens and disappears, the contamination particles on the windward and leeward sides of 2# insulator gradually fall off, and the increasing trend of contamination volume fraction of 2# insulator slows down.

#### 4.3. Different Wind Speeds

The wind speed has a crucial effect on the contamination characteristics on the insulator surface. With the wind speed of 25 m/s is used as an example to show the distribution of contamination on the insulator. The simulation conditions are set as follows: the particle size is 15  $\mu\text{m}$ , the particle concentration is 0.02  $\text{mg}/\text{m}^3$ , and the incoming flow is at the wind direction of  $90^\circ$ . The contamination distribution on the insulator surface is shown in Figure 20. Figure 21 presents (a) the contamination distributions on the windward side. (b) leeward side of 1# insulator. (c) the windward side. (d) leeward side of 2# insulator. Figures 22 and 23 show the curves of how the contamination volume fractions on various contact surfaces of the 1# insulator and the 2# insulator change with the wind speed.

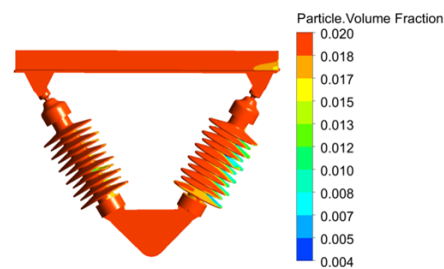


Figure 20. Distribution map of contamination on the surface of insulators.

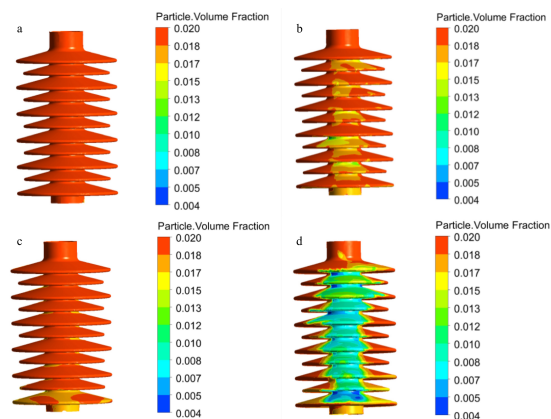
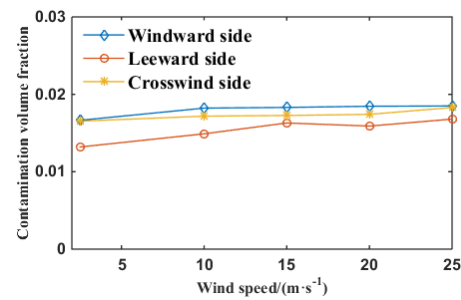
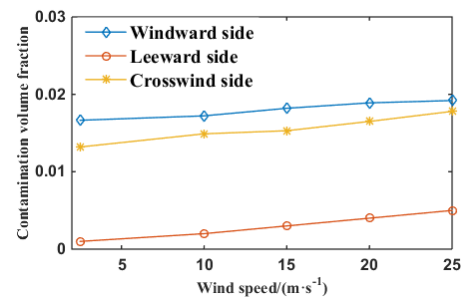


Figure 21. Distribution map of contamination on various sides of the insulator. (a) the contamination distributions on the windward side of 1# insulator; (b) the contamination distributions on the leeward side of 1# insulator; (c) the contamination distributions on the windward side of 2# insulator; (d) the contamination distributions on the leeward side of 2# insulator.



**Figure 22.** Contamination volume fraction of 1# insulator under different wind speeds.



**Figure 23.** Contamination volume fraction of 2# insulator under different wind speeds.

As can be seen from Figures 22 and 23, due to the same concentration of contamination particles in the spatial domain, the increased wind speed will make the collision between contamination particles and the insulator more intense, and the contamination volume fraction of the overall insulator surface will gradually increase with the increase of the wind speed. The overall contamination volume fraction of insulator is maintained within 0.02. The leeward side of the 1# insulator produces the primary wake flow. The vortex turbulence makes the contamination particles fall off the leeward side of the 1# insulator, which makes the contamination volume fraction slightly lower than that on the crosswind side, which is maintained at about 0.018 to 0.019. The leeward side of the 2# insulator produces the secondary wake flow. Because there is no shield behind it, the secondary wake flow gradually weakens, making the contamination particles on the leeward side fall off and become blown away by the wind. Its contamination volume fraction is the lowest, which is quite different from the contamination volume fractions on the windward and crosswind sides, and the maximum value is less than 0.005.

#### 4.4. Different Particle Sizes

The contamination particles are affected by both gravity and the flow field force. Gravity and flow field force on the contamination particles are related to the particle size. With a particle size of 10  $\mu\text{m}$  is used as an example to show the contamination distribution on the insulator. The simulation conditions are set as follows: the wind speed is 20 m/s, the particle concentration is 0.02  $\text{mg}/\text{m}^3$ , and the incoming flow is at the wind direction of 90°. The contamination distribution on the insulator surface is shown in Figure 24. Figure 25 shows (a) the contamination distribution on the windward side. (b) leeward side of 1# insulator. (c) the windward side. (d) leeward side of 2# insulator. Figures 26 and 27 show the curves of how the contamination volume fractions on various contact surfaces of the 1# insulator and the 2# insulator change with the particle size.

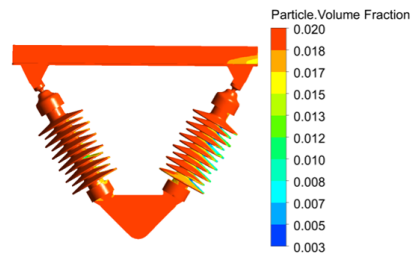


Figure 24. Distribution map of contamination on the surface of insulators.

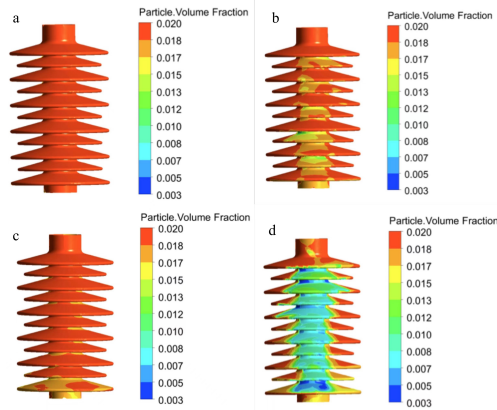


Figure 25. Distribution map of contamination on various sides of the insulator. (a) the contamination distributions on the windward side of 1# insulator; (b) the contamination distributions on the leeward side of 1# insulator; (c) the contamination distributions on the windward side of 2# insulator; (d) the contamination distributions on the leeward side of 2# insulator.

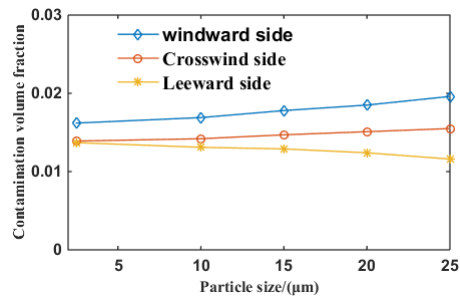


Figure 26. Contamination volume fraction of 1# insulator under different particle sizes.

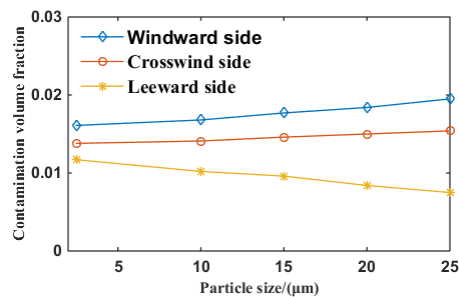


Figure 27. Contamination volume fraction of 2# insulator under different particle sizes.

As can be seen from Figures 26 and 27, with the increase of the contamination particle size, the contamination volume fractions on various contact surfaces of the 1# and 2# insulators showed a similar change trend. The 1# insulator contacts the wind first, the contamination fraction of its windward side gradually increases from about 0.016 to about 0.02. The leeward side of the 1# insulator produces the primary wake flow, and the contamination

particles detach from the 1# insulator and adhere to the windward side of the 2# insulator. The contamination volume fraction of the leeward side of 1# insulator gradually decreases from about 0.015 to around 0.01, while the contamination volume fraction of the windward side of 2# insulator increases from about 0.016 to about 0.02. The leeward side of the 2# insulator produces the secondary wake flow, which gradually weakens and disappears because there is no shield behind. The contamination particles on the leeward side fall off in large numbers, and the contamination volume fraction decreases from about 0.013 to around 0.008. With the increase of contamination particle size, the probability of collision with insulator surface increases, resulting in a noticeable growth trend of windward side. Larger particle size leads to a larger volume, and ultimately results in a larger mass. The heavier particles are more likely to detach from the insulator with the wake flow from the leeward side of the insulator, resulting in a decreasing contamination volume fraction on the leeward side.

#### 4.5. Different Angles of Incoming Flows

Different angles of incoming flows can not only affect the contamination characteristics of insulators, but also generate wakes with different directions and sizes. In this paper, five different angles of incoming flows are selected for simulation calculation:  $0^\circ$  wind direction angle,  $0^\circ$  wind elevation angle,  $30^\circ$  wind elevation angle,  $45^\circ$  wind elevation angle, and  $60^\circ$  wind elevation angle. The simulation conditions are set as follows: the wind speed is 20 m/s, the particle concentration is  $0.02 \text{ mg/m}^3$ , and the particle size is  $15 \mu\text{m}$ .

##### 4.5.1. Wind Direction Angle

Figures 28 and 29 show the front and back contamination distributions of insulator. Figures 30 and 31 show the cloud maps of the plane velocity distributions from the front view angle and the side view angle under the  $0^\circ$  wind direction angle.

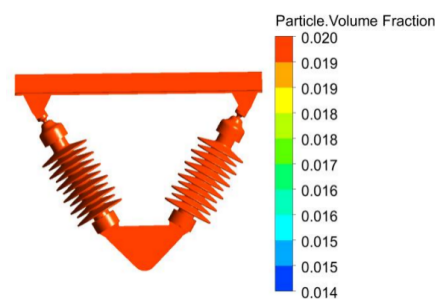


Figure 28. Distribution map of contamination on the front of insulators.

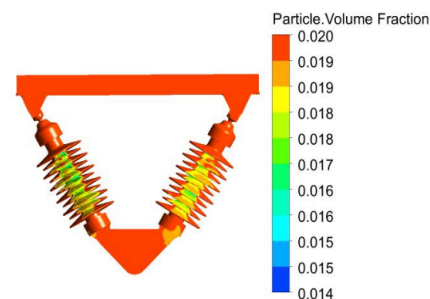
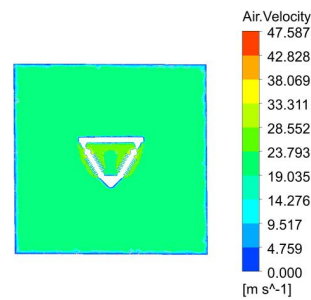
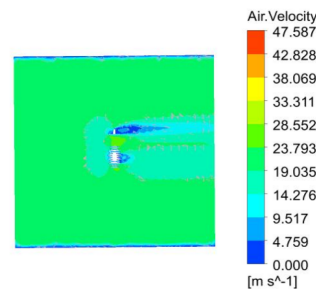


Figure 29. Distribution map of contamination on the back of the insulators.



**Figure 30.** Cloud map of plane velocity distribution at frontal viewing angle.



**Figure 31.** Cloud map of plane velocity distribution at the side view angle.

As shown in Figures 28 and 29, when the wind direction angle is  $0^\circ$ , the windward sides and the crosswind sides of the two insulators are the more contaminated. Because the leeward side of the insulator produces the wake flow, some contamination particles fall off from the leeward side and are blown away by the wind, and the contamination volume is small. It can be seen from Figures 30 and 31 that wind contacts the insulator on the windward side to create a boundary layer. Because there is a gap between the sheds, part of the incoming wind passes through the gap between the sheds; a strong wake flow is generated at the hanging shoulder frame, and a small wake flow at the insulator. Compared with a single insulator, when the incoming flow is at the prevailing wind direction of  $0^\circ$ , it is difficult to generate wake flow on the leeward side of the V-shaped double-suspension rod insulator, and in this case, the insulators have similar contamination characteristics to a single insulator. The windward side of the insulator is the most contaminated, and the leeward side has relatively less contamination. Therefore, focus should be more put on the windward and crosswind sides of the two insulators during insulator cleaning.

#### 4.5.2. Wind Elevation Angle

With the contamination distribution map on the surface of the insulator at a wind elevation of  $45^\circ$  as an example, the contamination distributions on the two insulators in our model are analyzed. The contamination distribution on the insulator surface is shown in Figure 32. Figure 33 demonstrates (a) the contamination distributions on the windward side of 1# insulator, (b) the contamination distributions on the leeward side of 1# insulator, (c) the contamination distributions on the windward side of 2# insulator, (d) the contamination distributions on the leeward side of 2# insulator. Under the  $0^\circ$  wind elevation angle,  $30^\circ$  wind elevation angle,  $45^\circ$  wind elevation angle, and  $60^\circ$  wind elevation angle, the cloud maps of plane velocity distributions are shown in Figures 34–37, Figure 38 presents the curves of how the contamination volume fractions of the 1# insulator and the 2# insulator change with the wind elevation angle.

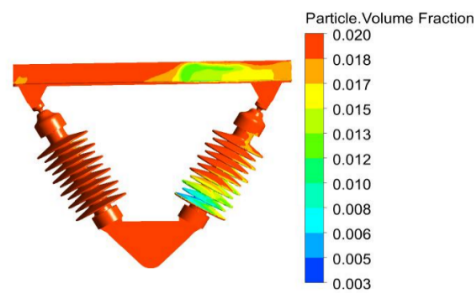


Figure 32. Distribution map of contamination on the surface of insulators.

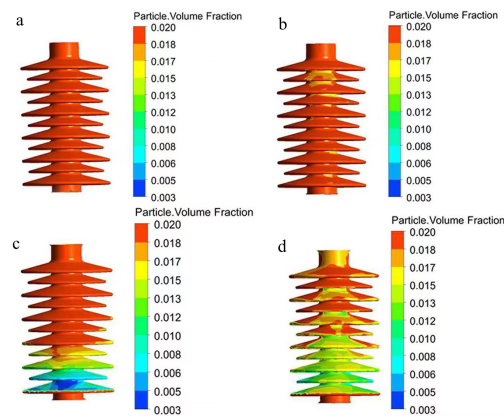


Figure 33. Distribution map of contamination on various sides of the insulator. (a) the contamination distributions on the windward side of 1# insulator; (b) the contamination distributions on the leeward side of 1# insulator; (c) the contamination distributions on the windward side of 2# insulator; (d) the contamination distributions on the leeward side of 2# insulator.

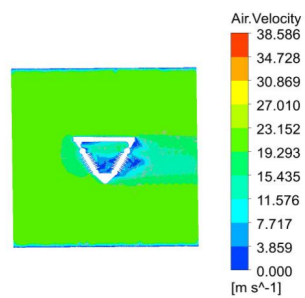


Figure 34. Cloud map of velocity distribution in the plane with 0° wind elevation angle.

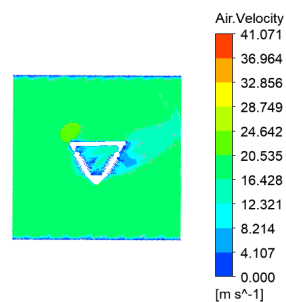


Figure 35. Cloud map of velocity distribution in the plane with 30° wind elevation angle.

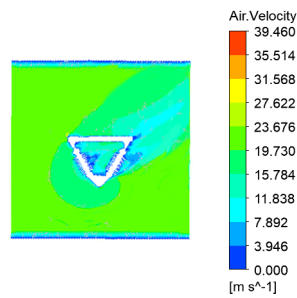


Figure 36. Cloud map of velocity distribution in the plane with 45° wind elevation angle.

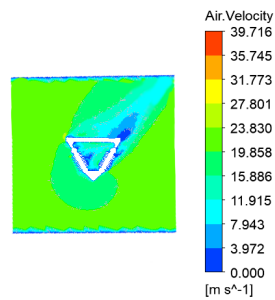


Figure 37. Cloud map of velocity distribution in the plane with 60° wind elevation angle.

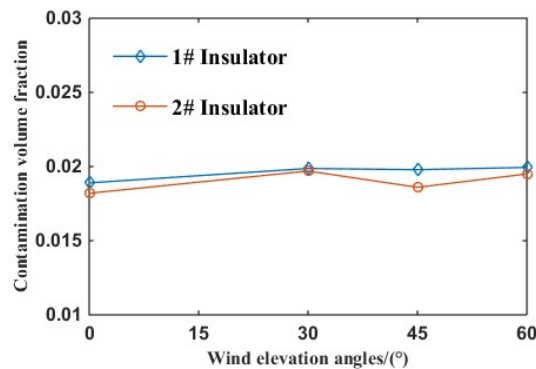


Figure 38. Contamination volume fractions of insulator under different Wind elevation angles.

As can be seen from Figures 34–37, the wake flow and continuation direction are consistent with the angle of incoming flow, and the wake flow continues backward with the airflow until it disappears. When airflow contacts the bluff-body, it tends to generate the wake flow. As shown in Figure 38, when the wind elevation angle is within the range of 0°~30°, the contamination volume fraction of insulator increases, and because the wind elevation angle is inclined downward for 1# insulator at this time, when it contacts the insulator, the contamination particles are more likely to adhere to it due to the obstruction on the upper surface of shed, resulting in an increase in contamination volume. When the wind elevation angle is in the range of 30°~45°, the contamination volume fraction of insulator is decreasing, because, at this time, the wind elevation angle is gradually getting close to being perpendicular to the 1# insulator, the incoming flow is blocked by the upper surface of the shed, and the surface contamination is gradually decreasing. When the wind elevation angle is in the range of 45°~60°, the contamination volume fraction of insulator is increasing. At this point, because the wind elevation angle is inclined upward for 1# insulator, when it comes into contact with the insulator, the contamination particles are more likely to adhere to it due to blocking by the lower surface of the shed, causing increase of contamination. When the incoming flow is at the prevailing wind elevation angle of 0°~60°, 1# insulator has the largest amount of contamination, and 2# insulator has the smallest amount of contamination on the leeward side. During insulator cleaning, more

focus should be put on the entire surface of 1# insulator and the windward and crosswind sides of 2# insulator.

### 5. Natural Contamination Experiment

The contamination of V-type double suspension rod insulators along the catenary of the Lanzhou-Xinjiang High-speed Railway are measured using the natural contamination method, and the experiment location was in the HongTai Station of the Lanzhou-Xinjiang High-speed Railway which is located in the “100 km wind area”. Taking ESDD and NSDD as parameters to characterize the degree of contamination. According to the field data, the erection direction of the insulator in catenary was north-south. There was north wind in March; that is, the wind came from the side with an elevation of  $0^{\circ}\sim 60^{\circ}$ . The experiment was conducted from March 1st to April 30th, lasting for 60 days. Figure 39 shows the pictures taken from four different angles during the experiment: (a) the windward side. (b) the Crosswind side 1. (c) the Crosswind side 2. (d) the Leeward side.

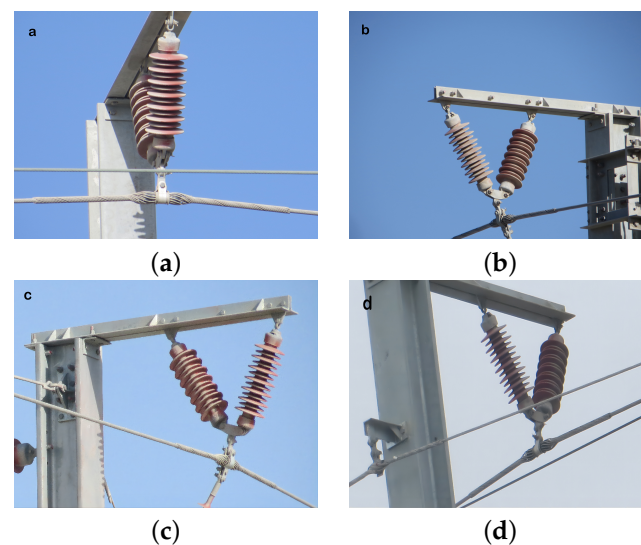


**Figure 39.** Pictures of the site. (a) Windward side; (b) Crosswind side 1; (c) Crosswind side 2; (d) Leeward side.

The experiment objects were divided into two groups, all of which were the V-type double-suspension rod insulators in the catenary along the Lanzhou-Xinjiang High-speed Railway. Before each experiment, both groups of insulators had been cleaned manually, and the surface contamination volume can be regarded as 0. After 60 days of experiment, the surface contamination of the insulator was collected, and ESDD and NSDD on the insulator surface were measured. In one experiment, the contamination was collected after 30 days of the experiment; in the other experiment, the contamination was collected after 60 days of the experiment. In each experiment, the experimental objects were both the two insulators.

The equivalent salt density (ESDD) and ash density (NSDD) are obtained by measuring the quality of insoluble materials collected from the insulator surface after dissolution, as shown in Table 1.

**Table 1.** ESDD and NSDD of two insulators.

V-type Double Suspension Rod Insulators/Experimental Group	ESDD/(mg·cm <sup>-2</sup> )		NSDD/(mg·cm <sup>-2</sup> )	
	1#	2#	1#	2#
Group 1	0.031	0.022	0.14	0.06
Group 2	0.047	0.034	0.18	0.09

According to the data in the table, in both experiments, the NSDD and ESDD distributions on the surface of 1# insulator were higher than the distributions on the 2# insulator. This verifies that the contamination distribution on the surface of 1# insulator was more than that on the 2# insulator when the incoming flow was from the side with an elevation of  $0^{\circ}\sim 60^{\circ}$ . Comparing the data of the two experiments, the distributions of NSDD and ESDD on the surface of the insulators in the second experiment were more than the distributions in the first experiment, which proves that the contamination on the insulator surface gradually increases with time. It can be seen from Figure 39a–d that when the incoming flow was from the side with an elevation of  $0^{\circ}\sim 60^{\circ}$ , the surface of 1# insulator presented a gray in general, and the color was darker than that of 2# insulator, which indicates that the contamination distribution on the surface of 1# insulator was denser than that of 2# insulator. This results are similar to the simulation results of  $0^{\circ}\sim 60^{\circ}$  wind elevation angle, which proves the rationality of the simulation process and results.

## 6. Discussion

The double-branched structure of the V-type double suspension rod insulators tends to form a wake in the flow field, while the wake seriously affects the pressure distribution and contamination distribution on the insulator surface. With gradual increase of the wind speed, the particle size and the particle concentration, the pressure and contamination distribution on the windward side of the two insulators will gradually increase. As a result, the primary wake flow will be generated on the leeward side of the 1# insulator, which affects the pressure on the crosswind and leeward sides of the 1# insulator, and the higher the pressure is, the more contamination is accumulated. Then, the secondary wake is generated on the leeward side of the 2# insulator. Since there is no obstruction behind it, the wake will gradually disappear and become an ordinary laminar flow. The direction and angle of the external flow field of the insulator are the same as the direction and angle of the wake generated by the insulator. The contamination accumulation test verifies the correctness of the conclusions drawn in this paper, and suggestions are also provided for the cleaning of insulators.

## 7. Conclusions

In this paper, the contamination accumulation simulation model is established based on the principle of fluid mechanics, the unstructured grids are divided, and three boundary conditions are set to carry out the fluid mechanics simulation experiments. Combined with the wake effects jointly generated by the two insulators in the flow field, the pressure distribution on the surface of the insulator, the contamination accumulation characteristics, the external flow field distribution of the insulator and the wake continuation direction under different influencing conditions are analyzed. The experimental results are similar to the simulation results. Therefore, the following important conclusions can be drawn for our study:

(1) Wake flow affects the static pressure on the insulator surface. The primary wake flow is gradually strengthened, causing the static pressure on the crosswind side of the 1# insulator to be lower than that on the leeward side; the secondary wake flow gradually weakens, resulting in little difference in static pressure between the leeward surface and the crosswind surface of the 2# insulator.

(2) The contamination volume fraction of the insulator is proportional to the contamination particle concentration and wind speed. Due to the influence of the primary wake flow, the contamination particles with larger particle sizes are more easily attached to the windward side of the 2# insulator and more easily fall off from the leeward side of the 1# insulator, resulting in a large difference between the contamination volume fractions of the two insulators.

(3) The wake flow direction is consistent with the angle of the external incoming flow, and the wake flow generating area will affect the surface contamination characteristics of the front and rear insulators, when the wake flow contacts the rear insulator, the secondary

wake flow will be generated, the unobstructed wake flow will gradually disappear, and the laminar flow will resume.

(4) When the incoming flow is at a prevailing wind direction of  $0^\circ$ , focus should be put on the windward and crosswind sides of the two insulators during insulator cleaning, and the contamination distributions on these two insulators are close; when the incoming flow is at a prevailing wind elevation of  $0^\circ \sim 60^\circ$ , focus should be put on the entire surface of 1# insulator and the windward and crosswind sides of 2# insulator during insulator cleaning.

**Author Contributions:** Conceptualization, T.W. and S.Z.; methodology, T.W.; software, T.W.; validation, T.W., S.Z. and Y.L.; formal analysis, T.W.; investigation, T.W.; resources, T.W., S.Z. and Y.Z.; data curation, T.W.; writing—original draft preparation, T.W.; writing—review and editing, T.W., S.Z. and Y.L.; visualization, T.W.; supervision, T.W.; project administration, T.W.; funding acquisition, S.Z. All authors have read and agreed to the published version of the manuscript.

**Funding:** This work was supported in part by the National Natural Science Foundation of China (Grant No. 51867013), in part by the National Natural Science Foundation of China (Grant No. 51767014), in part by the National Natural Science Foundation of China (Grant No. 51567014). and by the Tianyuo innovation team plan of Lanzhou Jiaotong University (TY202010).

**Institutional Review Board Statement:** Not applicable.

**Informed Consent Statement:** Not applicable.

**Data Availability Statement:** Not applicable.

**Conflicts of Interest:** The authors declare no conflict of interest.

## References

- Liu, H.; Quan, Y.S.; Chen, N.; Shi, P.X. The Influence of Main Components in PM<sub>2.5</sub> on Composite Insulator Contamination Flashover Characteristics. In *Applied Mechanics and Materials*; Trans Tech Publications Ltd.: Bäch, Switzerland, 2014; Volume 672, pp. 827–830.
- He, J.; Gorur, R. A probabilistic model for insulator flashover under contaminated conditions. *IEEE Trans. Dielectr. Electr. Insul.* **2016**, *23*, 555–563. [[CrossRef](#)]
- Gao, S.; Tao, F.B.; Liu, Z.Y.; Zhou, Z.C.; Wang, L.M. A Study on Porcelain Insulator Flashover Voltage Evaluation System on Atmospheric Pollution Condition. In *Advanced Materials Research*; Trans Tech Publications Ltd.: Bäch, Switzerland, 2014; Volume 1008, pp. 610–614.
- Tan, B.; Yue, Y.; Chen, X.; Huang, F.; Cheng, Z.; Chao, Y.; Sun, Z.; Zou, Y. Research on online diagnosis method of insulator contaminated discharge based on XGBoost algorithm. In *Journal of Physics: Conference Series*; IOP Publishing: Bristol, UK, 2021; Volume 2035, p. 012001.
- He, L.; Gorur, R. Source strength impact analysis on polymer insulator flashover under contaminated conditions and a comparison with porcelain. *IEEE Trans. Dielectr. Electr. Insul.* **2016**, *23*, 2189–2195. [[CrossRef](#)]
- Stefenon, S.F.; Ribeiro, M.H.D.M.; Nied, A.; Mariani, V.C.; Coelho, L.D.S.; Leithardt, V.R.Q.; Silva, L.A.; Seman, L.O. Hybrid wavelet stacking ensemble model for insulators contamination forecasting. *IEEE Access* **2021**, *9*, 66387–66397. [[CrossRef](#)]
- Ramesh, M.; Gorur, R. Stretched grid finite difference method for computation of electric field in composite insulators with defects. *Electr. Power Syst. Res.* **2021**, *192*, 106875. [[CrossRef](#)]
- Cao, B.; Wang, L.; Yin, F. A low-cost evaluation and correction method for the soluble salt components of the insulator contamination layer. *IEEE Sens. J.* **2019**, *19*, 5266–5273. [[CrossRef](#)]
- Conner, J.; Lantz, A. The insulator contamination problem as influenced by silicone surface coatings. *Trans. Am. Inst. Electr. Eng. Part III Power Appar. Syst.* **1958**, *77*, 1101–1106. [[CrossRef](#)]
- Shariati, M.R.; Moradian, A.R.; Vaseai, S.J.A.; Kamali, S.A.; Niroo Rseearch Institute; Alizadeh, G.; Hormozgan Regional Electric Co. Iran Examines Insulator Contamination. *Transmission & Distribution World*. 2008. Available online: <https://www.tdworld.com/overhead-transmission/article/20961113/iran-examines-insulator-contamination> (accessed on 9 August 2022).
- Yang, Z.; Jiang, X.; Han, X.; Zhang, Z.; Hu, J. Influence of pollution chemical components on AC flashover performance of various types of insulators. *High Volt.* **2019**, *4*, 105–112. [[CrossRef](#)]
- Kontargyri, V.; Gialketsi, A.; Tsekouras, G.; Gonos, I.; Stathopoulos, I. Design of an artificial neural network for the estimation of the flashover voltage on insulators. *Electr. Power Syst. Res.* **2007**, *77*, 1532–1540. [[CrossRef](#)]
- Shariatinasab, R.; Saghafi, S.; Khorashadizadeh, M.; Ghayedi, M. Probabilistic assessment of insulator failure under contaminated conditions. *IET Sci. Meas. Technol.* **2020**, *14*, 557–563. [[CrossRef](#)]
- Vita, V.; Ekonomou, L.; Chatzarakis, G.E. Design of artificial neural network models for the estimation of distribution system voltage insulators' contamination. In Proceedings of the 12th WSEAS International Conference on Mathematical Methods, Computational Techniques and Intelligent Systems, Sousse, Tunisia, 3–6 May 2010; pp. 3–6.

15. Thanh, P.N.; Cho, M.Y.; Da, T.N. Insulator leakage current prediction using surface spark discharge data and particle swarm optimization based neural network. *Electr. Power Syst. Res.* **2021**, *191*, 106888. [[CrossRef](#)]
16. Gencoglu, M.T.; Uyar, M. Prediction of flashover voltage of insulators using least squares support vector machines. *Expert Syst. Appl.* **2009**, *36*, 10789–10798. [[CrossRef](#)]
17. Zhang, C.; Hu, J.; Li, J.; Liu, D.; Wang, L.; Lu, M. Experimental study on the contamination deposition characteristics of insulators in a fog–haze environment. *IET Gener. Transm. Distrib.* **2018**, *12*, 406–413. [[CrossRef](#)]
18. Jiang, Z.; Jiang, X.; Guo, Y.; Hu, Y.; Meng, Z. Pollution accumulation characteristics of insulators under natural rainfall. *IET Gener. Transm. Distrib.* **2017**, *11*, 1479–1485. [[CrossRef](#)]
19. Lv, Y.; Li, J.; Zhang, X.; Pang, G.; Liu, Q. Simulation study on pollution accumulation characteristics of XP13-160 porcelain suspension disc insulators. *IEEE Trans. Dielectr. Electr. Insul.* **2016**, *23*, 2196–2206. [[CrossRef](#)]
20. Zhang, Z.; Lu, B.; Fu, H.; Liu, J.; Wu, J. Characterization of insulator contamination based on XP-160 pollution volume fraction. *Power Syst. Technol.* **2020**, *45*, 3737–3744.
21. Dong, H.; Zhang, Y.; Dong, H. Electric Field Characteristics Analysis of Contaminated Composite Insulator Based on 3-D Model. *J. Lanzhou Jiaotong Univ.* **2019**, *38*, 46–51. 57.
22. Li, J.; Jiang, Y.; Lu, M.; Liu, Z.; Hua, K.; Li, Z. Study on the difference of chemical composition of insulator contamination on UHV-AC and-DC transmission lines. *IET Sci. Meas. Technol.* **2018**, *12*, 17–24. [[CrossRef](#)]
23. Gao, B.; Yang, F.; Songyang, Z.; Degui, Y.; Xiaokuo, K.; Zehui, L.; Chao, L. The movement characteristics of charged haze particles in ionized field and its influence on contamination of insulator. *IEEE Trans. Magn.* **2017**, *54*, 1–4. [[CrossRef](#)]
24. Yang, J.; Mei, H.; Zhang, F. Simulation study on contamination accumulation characteristics of insulator by feature particle tracking method. *High Volt. Appar.* **2020**, *56*, 124–132. 140.
25. Te, L.; Shaohua, W.; Haojun, L.; Yangyong, X.; Yuntu, J.; Peng, J. Comparison of natural contamination accumulation characteristics between composite rod insulators and standard suspended insulator strings. *J. Eng.* **2019**, *2019*, 1027–1032. [[CrossRef](#)]
26. Huang, Y.; Huang, X. Flow field distribution around insulator and contamination uneven characteristic of insulator. *IET Sci. Meas. Technol.* **2020**, *14*, 1088–1097. [[CrossRef](#)]
27. Haddadi, H.; Shojaei-Zadeh, S.; Connington, K.; Morris, J.F. Suspension flow past a cylinder: particle interactions with recirculating wakes. *J. Fluid Mech.* **2014**, *760*. doi:10.1017/jfm.2014.613. [[CrossRef](#)]
28. Zhang, L.; Li, L. Application of Bernoulli Equation in Fluid Mechanics. In *Advanced Materials Research*; Trans Tech Publications Ltd.: Bäch, Switzerland, 2013; Volume 774, pp. 335–339.
29. Li, H.A.; Zhang, M.; Yu, K.; Qi, X.; Hua, Q.; Zhu, Y. R3MR: Region growing based 3D mesh reconstruction for big data platform. *IEEE Access* **2020**, *8*, 91740–91750. [[CrossRef](#)]
30. Zhang, X.; Fan, C.; Guo, Y.; Liu, K.; Liu, Y.; Wu, G. Microscopic Distribution of Polluted Particles on the Surface of Insulating Materials. *Power Syst. Technol.* **2019**, *44*, 1180–1187.
31. Laptinskii, V. Exact Solution of the Prandtl Problem about a Dynamic Laminar Boundary Layer. *Differ. Equ.* **2020**, *56*, 538–542. [[CrossRef](#)]